36B-L.0 RATIONALIZATION OF LIQUID/SOLID AND SOLID/SOLID INTERFACE INSTABILITIES DURING THERMAL-MECHANICAL TRANSIENTS OF METAL ADDITIVE MANUFACTURING

Katie O'Donnell, Matthew Kenney, Amamchukwu Ilogebe, Maria Quintana (ISU)
Faculty: Peter Collins (ISU)
Industrial Mentor: Billy Short and Jennifer Wolk (ONR)

This project initiated in Fall 2018 and is part of a Multiple University Research Initiative (MURI) supported by ONR. The research performed during this project will serve as the basis for Ph.D. theses for Katie O'Donnell and Amamchukwu Ilogebe and a Master's thesis for Matthew Kenney.

36B-L.1 Project Overview and Industrial Relevance

The length and time scales in additive manufacturing (AM), as compared to other manufacturing techniques such as welding, casting, powder metallurgy, etc., create unique relationships between the resulting thermal gradients and microstructure. The goal of this project is to understand the science behind the relation between thermal gradients in AM builds, as a function of different scan strategies, and the microstructure and texture evolution, using Ti-6Al-4V, and Inconel 738, and Haynes 282.

Understanding the underlying behavior of different AM strategies on resulting microstructure and mechanical properties of metallic printed parts can help with optimizing the final cost and mechanical properties of AM components. In addition, another benefit of the project is the generation of data for Integrated Computational Materials Engineering (ICME) models, especially in known AM gap areas (nano and micro scale regimes of length and time).

36B-L.2 Previous Work (Work that was done since the beginning of the project, or literature review)

Past results have revealed that it is possible to vary the material state (microstructure and texture) by modifying the scanning strategy for electron beam powder bed additive manufacturing (Figs. 36B-L.1 and 36B-L.2). The microstructures that are observed are consistent with those expected for Ti-6Al-4V. Electron backscatter diffraction (EBSD) results (Fig. 36B-L.2) showed that there is a [001] growth texture in the parent beta grains, and the solid-solid phase transformation results in α laths that are consistent with the Burger's orientation relationship. Variations in the percentage basketweave and colony (Table 36B-L.1) indicate the importance of time between thermal cycles that permits the sample to cool more (for the raster-line scan strategy), resulting in higher cooling rates across the beta transus. For these samples, with rectilinear geometries, they seem to reach a 'steady state' by the center of the builds (~12.5 mm in height). The Dehoff strategy with specific melting sequence and parameters (dwell time and current) creates a material with the highest texture of the three, while the microstructural features (common variant packet size and colony fraction) are a midpoint between those obtained with raster and random strategies.

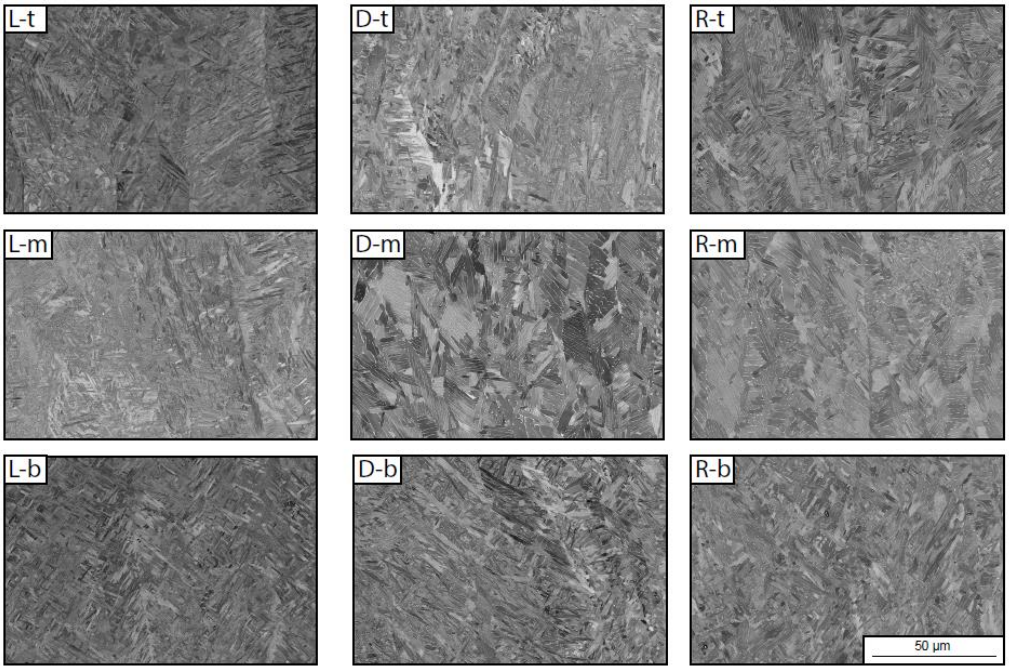

Figure 36B-L.1. Scanning Electron images of all 3 samples at the 3 specified locations. L – raster, D – Dehoff, R – random, t – top, m – middle and b - bottom

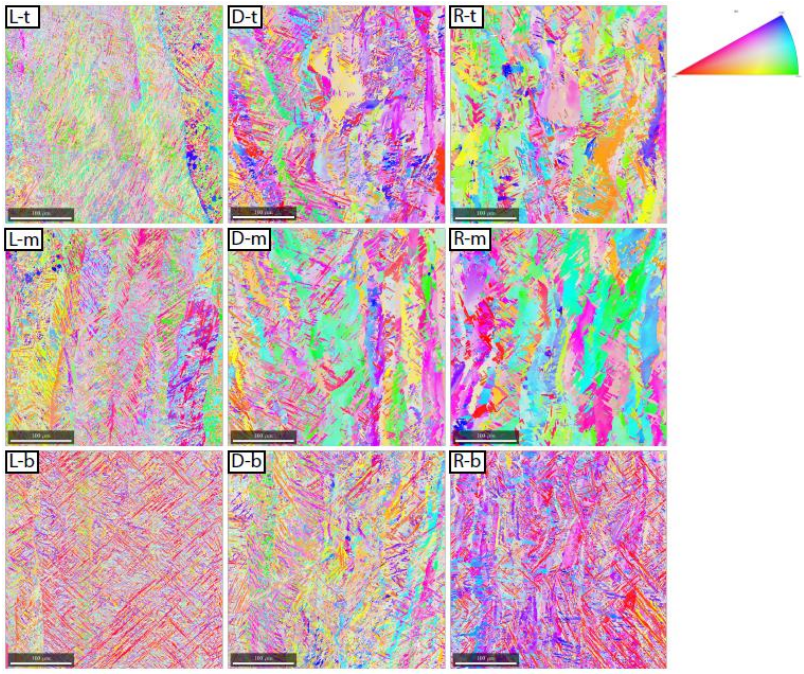

Figure 36B-L.2. Electron Backscatter Diffraction IPF-z maps of all three samples for α at the three specified locations. L – raster, D – Dehoff, R – random, t – top, m – middle and b – bottom

Table 36B-L.1: Measurements of common variant packet size, colony scale factor, colony volume fraction, and alpha lath width obtained from IPF maps and SEM images with corresponding sample location

Sample-location	Colony Scale Factor [µm]	Common Variant Packet size [µm]	Volume fraction colony [%]	α lath width [µm]
L-b	12.8	5.3	1.8	1.48
L-m	9.4	6.4	2.9	1.51
L-t	11.2	5.5	2.1	1.48
D-b	10.5	6.9	2.8	1.56
D-m	13.4	9.8	20.2	1.59
D-t	14.1	8.2	16.3	1.57
R-b	11.2	6.8	4.3	1.52
R-m	22.6	16.7	35.6	1.61
R-t	18.0	11.6	49.6	1.60

X-ray CT analysis (Fig. 36B-L.3) of a small volume of unused powder shows the existence of internal porosity within unused powder particles, supporting the current theory that entrapped argon gas pockets likely exist in the powder. These gas pockets can be responsible for porosity observed in the parts, if the AM process (i.e., the combination of scanning strategy and processing parameters) does not fully melt the particles or does not allow for adequate convective and surface tension conditions for these gasses to escape the melt pool. The equivalent diameter of the pores measured in the parts was found to be in the ~1 µm to ~50 µm range for all three scanning strategies.

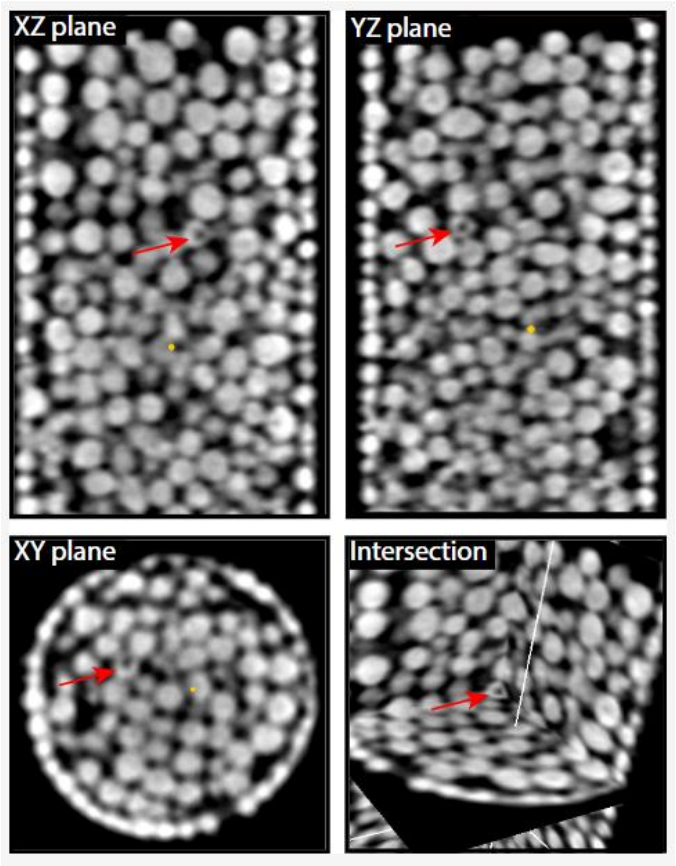

Figure 36B-L.3. X-ray CT data of analyzed powder showing one particle with internal porosity in different views

Once present in the deposited material, the characteristics of the observed pores point to several interesting phenomena present in the additive manufacturing process. The first is that instead of pores having a smooth surface, there are perturbations that disrupt the free surfaces of the pores (see the slightly tilted horizontal lines inside the pore in Fig. 36B-L.4a). These perturbations are nearly orthogonal to the build direction (which runs vertically in these images and is labeled with an arrow showing +z). They are not associated with structural remodeling of the surface due to the expected solid-state phase transformations in Ti-6Al-4V (i.e., β→α or β→α'), which manifest themselves as finer microstructural features surrounding the pores (see Fig. 36B-L.4b). The second observation is that pores with perturbations normal to the vertical sidewalls exhibit a vertical compression and their shapes become less spherical and more oblate in nature. Qualitatively, the pores also tend to have a rougher bottom surface (with more kinks, steps, or flatter shapes), whereas the top tends to better retain the hemispherical dome (see the round top half and the flatter bottom with horizontal perturbations in Fig. 36B-L.4c). However, these two characteristics, sidewall perturbations and vertical compression, were primarily observed in pores with a diameter in the higher range (i.e., pores with diameters >25μm). Smaller pores tended to have different geometric structures that reflected the scale of the surrounding 2-phase microstructures and were more spherical in nature (see Fig. 36B-L.4d). Regarding the size distributions, the large pores (i.e., the ones presenting compression and perturbations) were only observed in the raster scan strategy. The two spot melting strategies (D and R) did not contain any pore larger than 25μm. This means the kinetics, thermodynamics, and geometry of the melt pool play an important role in generating conditions in point melting strategies for large gas bubbles to escape and avoid becoming gas pores when solidification takes place, consistent with the literature [36B-L.1-36B-L.3].

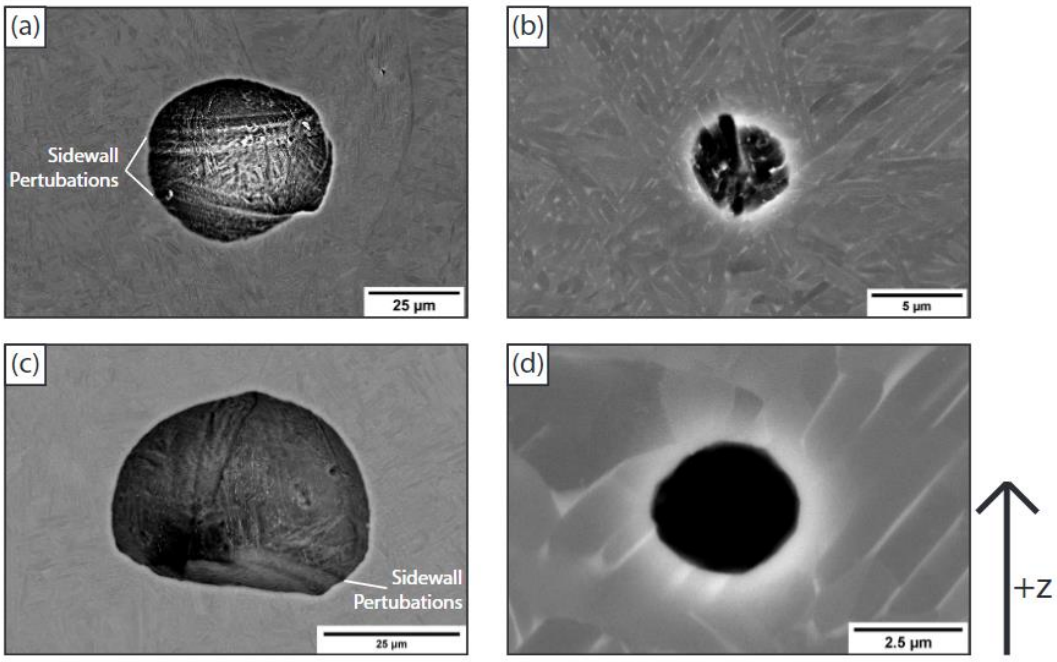

Figure 36B-L.4. Spherical porosity found within the samples, (a) a large spherical pore showing horizontal sidewall perturbations from sample L (location: top third, center), (b) fine surface features as a result of the solid-state phase transformation of Ti-6Al-4V.

The transformed alpha and beta microstructure surrounding these pores does not appear deformed, suggesting that the deformation/buckling of the pores occurred in the beta phase during thermal contraction and before the solid-state phase transformation to the final α + β microstructure. An EBSD scan of the microstructure around one spherical pore is presented in Figure 36B-L.5. EBSD results are particularly sensitive to stored dislocation densities from plastic deformation leading to a broadening of the Kikuchi bands in the electron backscattered patterns and slight crystallographic rotations within a grain containing excess dislocations [36B-L.4-36B-L.6]. These phenomena are absent from the buckled regions, strongly suggesting that the alpha laths formed after the material had already buckled.

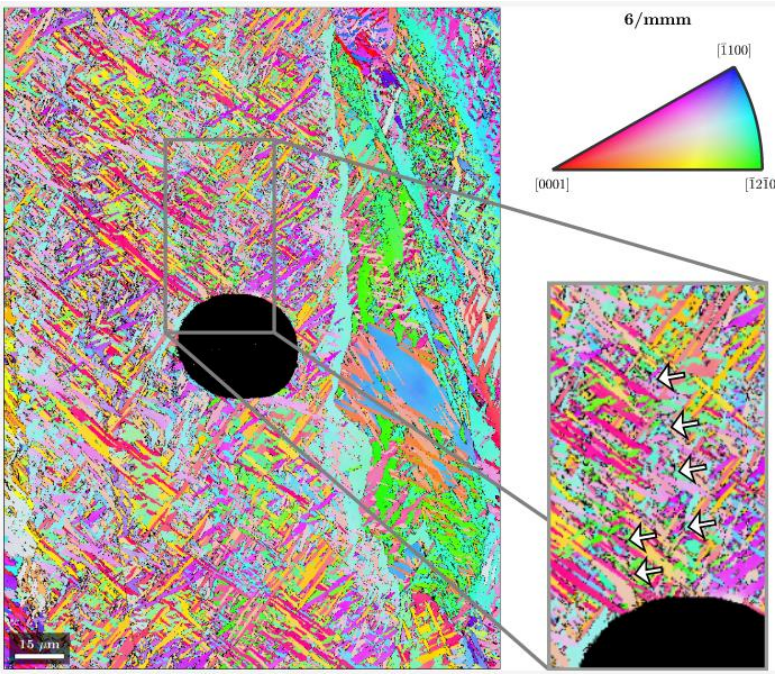

Figure 36B-L.5. EBSD of a spherical pore (sample L) close to a prior beta grain boundary, and a close up showing unindexed pixels (arrows) and slight crystallographic rotation of the alpha laths above the pore

EDS analysis of the samples have shown chemical variations in the material, corresponding with microstructural banding previously observed with optical microscopy. The variation in composition, and thus the microstructural banding, seems to be a result of a combination of preferential vaporization of aluminum from the surface of melt pools and solute segregation. Work initially began on studying the variations around spherical porosity, but has expanded to show that the variations exist throughout the part, including scans conducted around LOF defects and in regions which contain no defects. The variations have also been shown to exist across scan strategies, present in the raster sample as well as both point-melting samples.

Fig. 36B-L.6a shows chemical variations corresponding with microstructural banding. Figs. 36B-L.6b-36B-L.6e show compositional fluctuations around spherical porosity, paired with SEM images of the pores. It is noteworthy that the fluctuations in aluminum content are not symmetrical and seem to be interacting with the upper surface of the pore, possibly due to capillary forces and fluid flow differences between liquid properties generated by the compositional gradient. Similar results were observed in several other regions across the samples.

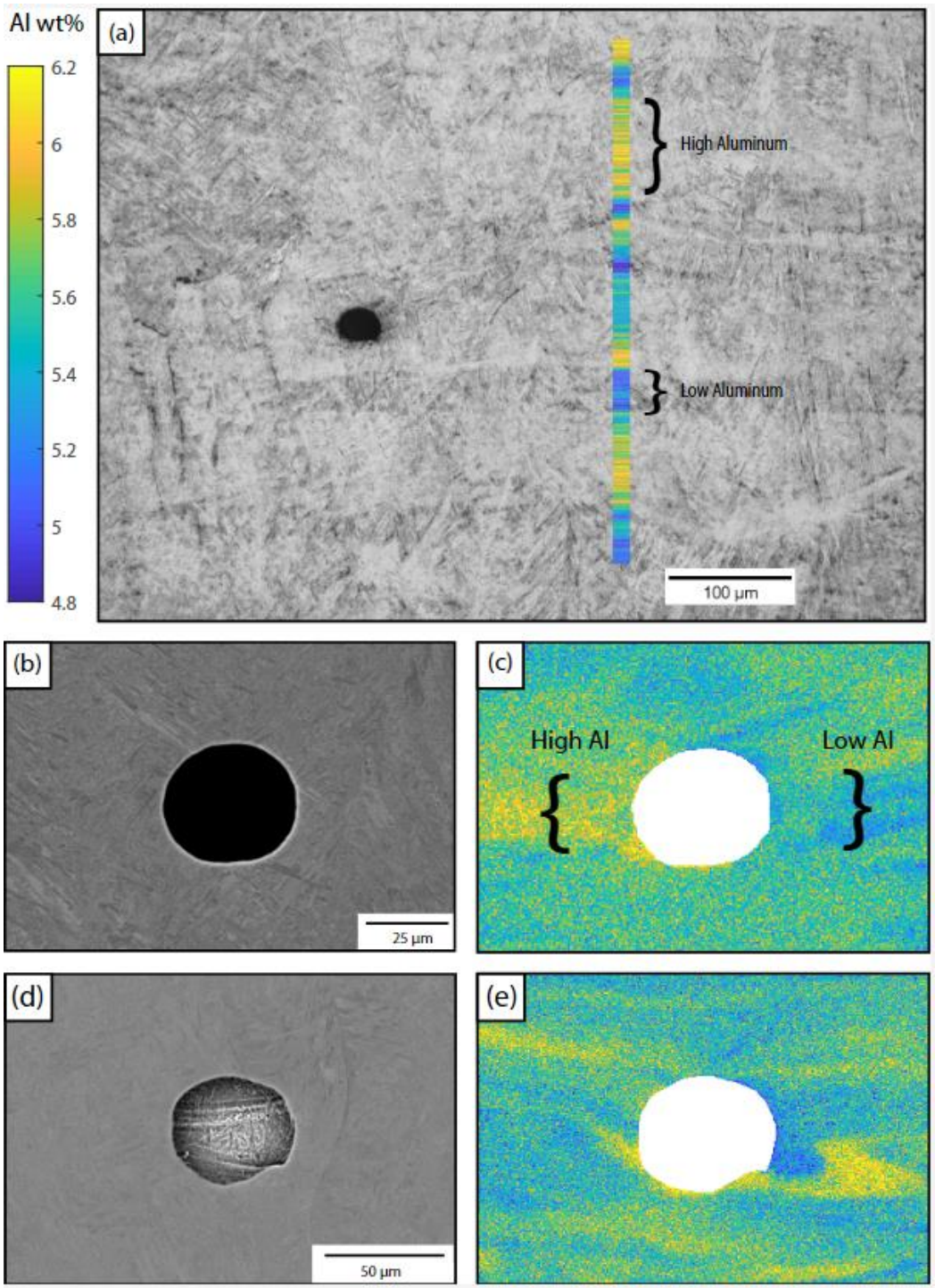

Figure 36B-L.6. Compositional variations near spherical pores in sample L. (a) Optical micrograph showing a gas pore and banding corresponding to low Al bands (dark gray) and high Al bands (light gray), (b) BSE image of a pore paired with its EDS map (c) that also show Al-rich zones (yellow) and Al-lean zones (blue) (location: top third, edge) and (d) BSE image of a larger area surrounding the pore shown in Fig. 2a paired with its EDS map (e) showing compositional variations matching with the kink in the bottom right edge of the pore, and non-homogeneous mixing on the left side of the image (location: top third, center). The Al wt% range is the same for all maps in this figure.

36B-L.3 Recent Progress (Work that has been completed since the last meeting)

Recent progress has been focused into three tasks: finite element model of stress fields influencing spherical pores and their buckling considering other variables (pore size, chemical variations, interactions between pores, thermal gradients), preliminary microstructural analysis of Haynes 282 and Inconel 738 samples, initial local property variation experiments to correlate with the previous EDS mapping, and parent β grain reconstruction.

36B-L.3.1 Continued FE Modeling

To further analyze the previously obtained results regarding structures and morphologies of spherical pores, COMSOL simulations have continued to be carried out. The intent of these simulations is to obtain the stress field on the surface of a gas pore under a thermal gradient. Variables included in the simulations include the modeling presence of compositional variations through property variations, the effect of thermal gradient (by varying the size of the matrix and the temperature fields), the effect of the size of porosity, and the effect of the presence of nearby pores. All simulations consider Ti-6Al-4V as the surrounding matrix and argon as the material within the sphere. For compositional fluctuations, the elastic modulus in the surrounding material (left and right) was varied by +/-5% to either side of the simulated pore. For the model depicted in Fig. 36B-L.7, the thermal gradient was 1.2°C/µm, the pore itself has a diameter of 30µm, and the matrix was constructed in the form of a 500µm x 500µm x 500µm cube. The bottom surface of the cube was considered as a fixed constraint, and temperature appropriate thermal conditions were applied to generate the aforementioned thermal gradient. The gradient itself was chosen from a combination of knowledge of the thermal properties and phase transition temperatures of Ti-6Al-4V and of thermal gradients in EBM Ti-6Al-4V [36B-L.7]. Equations for temperature dependent properties of Ti-6Al-4V were taken from [36B-L.8].

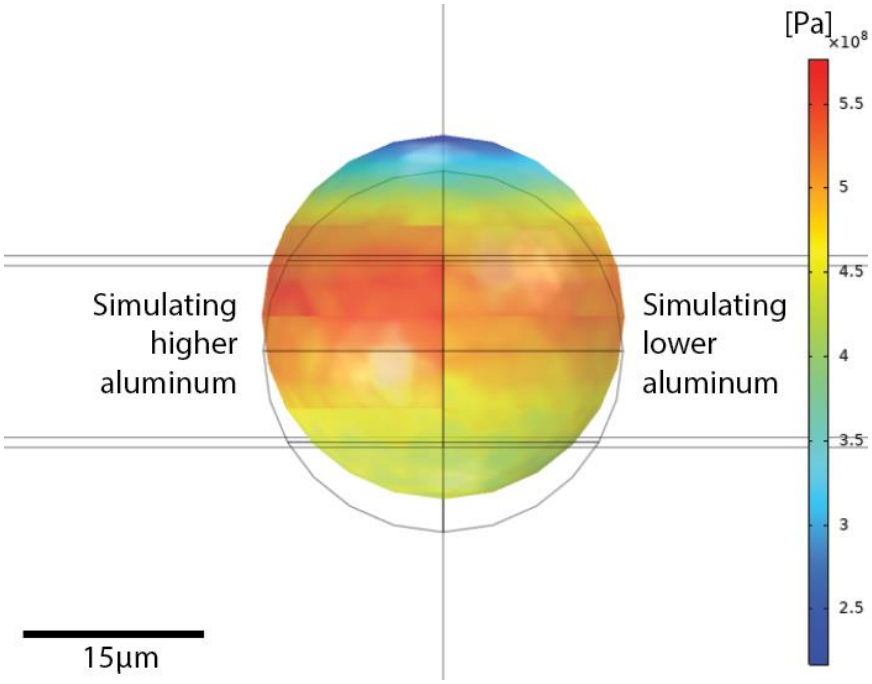

Figure 36B-L.7. Two-dimensional view of the Von Mises stress distribution inside a pore generated by finite element simulation of differences in the elastic modulus in both sides of a pore as a result of chemical instabilities caused by the AM process.

Results of a designed experiment, examining the influence of thermal gradient, pore location within a matrix, and pore size, has shown that the influence of thermal gradient on the resulting stress on the pore is not statistically significant when compared with the temperature field the pore might be contained in. Said design of experiment also showed that statistical significance only exists between the largest and the smallest of pore sizes (here, 5 vs 50µm

diameters), thus, moving forward, COMSOL simulations including the influence of pore size on the resulting maximum stress on a pore can be limited to only two pore diameters, rather than the range previously used. An example of the results from this designed experiment is shown in Fig. 36B-L.8.

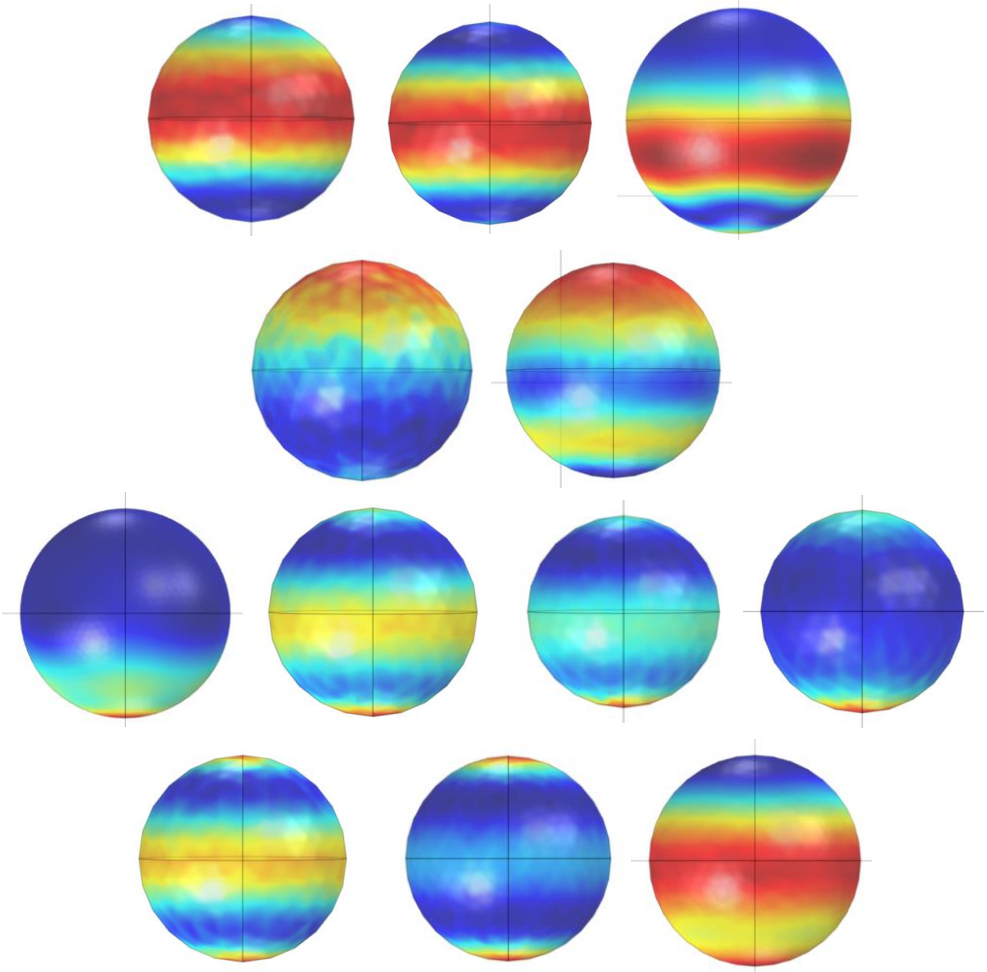

Figure 36B-L.8. Two-dimensional view of the Von Mises stress distribution for the designed thermal gradient experiments, showing the different stress distribution types. The first five were observed on at 2/3^{rds} of the matrix height, while the remaining seven were observed at either 1/2 or 1/3 of the matrix height.

36B-L.3.2 Haynes 282 Microstructure

The Haynes sample was explicitly designed with inbuilt cuboid pores and three wall struts with different thicknesses using a raster EBM scanning pattern. The specimen is 20 x 20 x 30mm with a 3 x 3mm cuboid and thin wall struts of 2mm, 3mm, and 4mm. The cuboidal pores were built-in to study the effect of thermal gradient on the microstructure and texture of the alloy around sizable pores. At the same time, the struts with different diameter specimen will aid the understanding of process-structure relationships to the size of the manufactured part. The sample was sectioned along the XZ-plane (parallel to the build direction) to expose the inbuilt cuboid pores and bisect the struts into two parts.

Microstructure

The SEM images show microstructure with columnar grains aligned parallel to the build direction, as shown in figure 1a. This type of structure is typical of EBM processed Ni-based superalloys due to the high rate of heat extraction parallel to the build direction [36B-L.9]. The characteristic of epitaxial solidification observed in the

microstructure is associated with the thermal gradient along the build direction [36B-L.10, 36B-L.11]. However, equiaxed grains were present at the top of the inbuilt cuboid, resulting from new grain nucleation. There is also an equiaxed-columnar transition after about 500 microns from the top of the cuboids, shown in figure 1b.

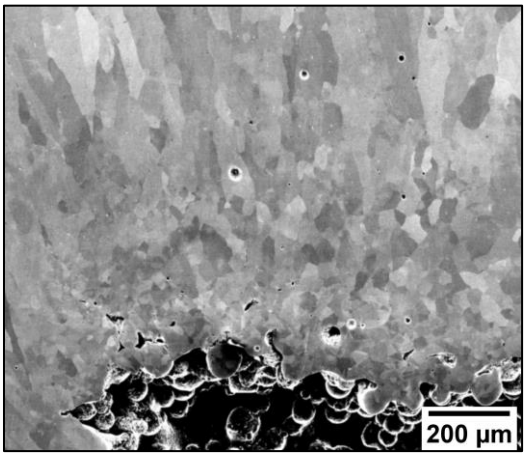

Figure 36B-L.9. Haynes 282 microstructure showing columnar grains parallel to the build direction along with an equiaxed-columnar grain transition at the top of inbuilt cuboid pore.

Precipitates

The scanning electron micrographs show primarily two significant strengthening precipitates. These are carbides and gamma prime, as illustrated in figures 2(a) and 2(b), respectively. The gamma prime precipitates are randomly distributed across the sample. The γ' at the bottom of the build possess more of a cuboidal shape compared to spherical shapes observed with γ' at the top. Figure 2(a) shows intragranular and grain boundary carbides. Previous researches on this alloy suggested that these carbides are MC-type primarily associated with Titanium and Molybdenum [36B-L.9, 36B-L.12]. The next step would include EDS analysis to verify the composition of the carbide precipitates and further characterize the gamma prime precipitate.

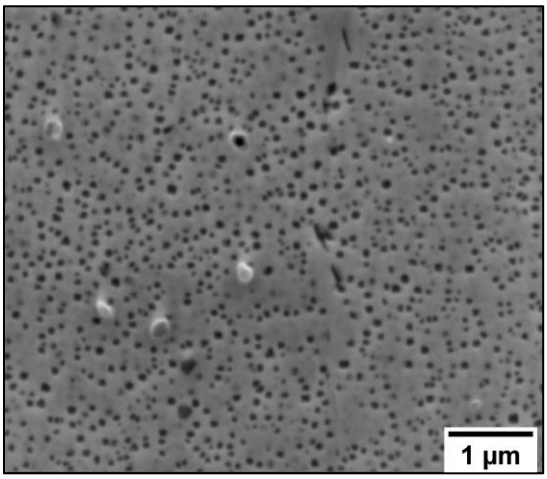

Figure 36B-L.10. EBM Haynes micrograph showing carbide precipitates and gamma/gamma prime precipitates

Defects

There are two main types of defects observed in the EBM Haynes 282, process-induced and powder-induced defects. The spherical pores are suspected to be associated with the entrapped gas in the gas atomized powder during powder production [36B-L.13]. The process-induced defects include hot tearing parallel to the build direction, which could have resulted from the incomplete flow of metal into the desired melt region. This type of defect is sometimes

called shrinkage porosity [36B-L.14]. Detailed analysis will be conducted to determine the percentage distribution of these defects along the build direction.

36B-L.3.3 Local property variations

Initial nanoindentation work has been completed on a randomly selected region of the raster Ti64 sample, with the intent of correlating any existing local property variations with the already established compositional variations. Preliminary results are shown in Fig. 36B-L.8. From this initial data, the banding clearly observed in both optical microscopy and EDS maps is not present. However, these results have yet to be directly correlated to EDS results.

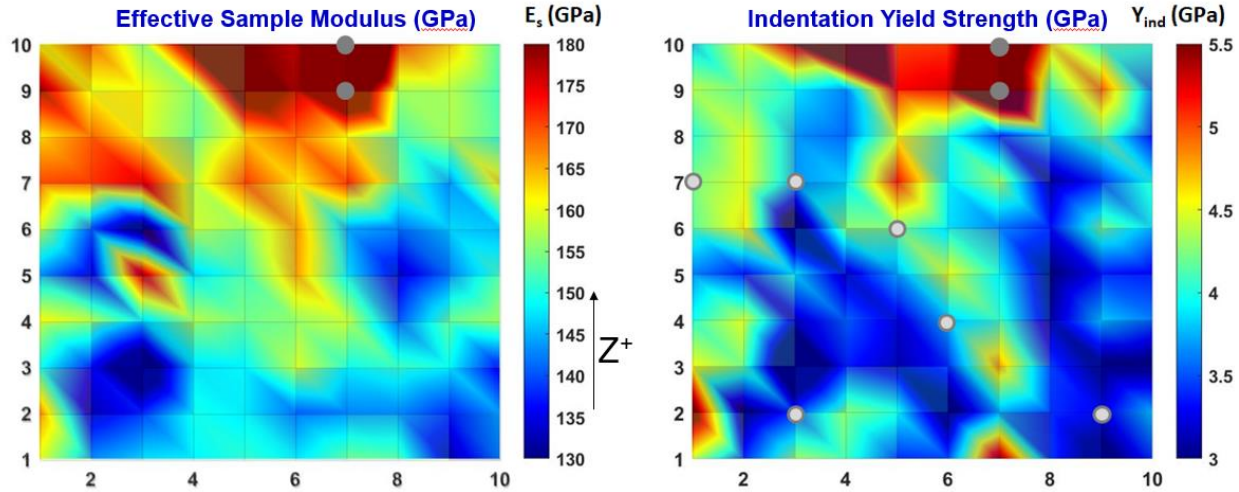

Figure 36B-L.11. Initial nanoindent data. Data represents a 10x10 grid, with indents spaced 10µm apart. Gray circles represent uncertain or bad modulus data; white circles represent bad yield data (large pop-ins), with interpolated values based on neighboring tests used for the plot.

Preliminary microhardness tests have also been carried out, with initial analysis showing a correlation between aluminum content and hardness value. These results are shown in Fig. 36B-L.9.

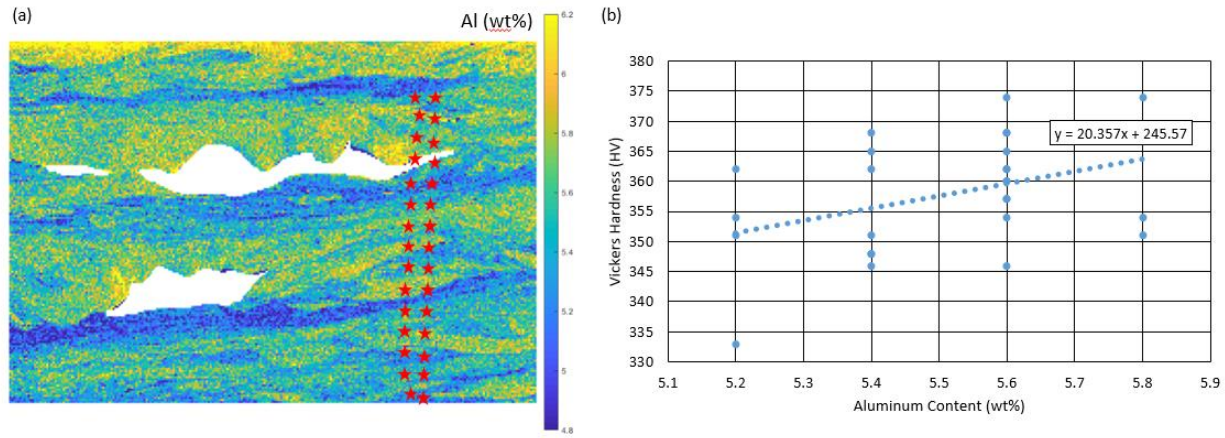

Figure 36B-L.12. Preliminary microhardness results with (a) showing the location of hardness indents and (b) showing a qualitative assessment of the aluminum content at each hardness location. Indents overlapping with the LOF shown in (a) were not included in the data analysis.

36B-L.3.4 Parent β grain reconstruction

Using MTEX/MATLAB software, reconstruction of the parent β grains in the Ti64 samples has begun to be carried out. This reconstruction thus far has been primarily focused on regions containing defects, showing the way that larger defects can affect grain growth, particularly columnar grain growth. Such defects can act as thermal barriers, stopping columnar growth at their floors and leading to nucleation of new grains at their ceilings. Overhanging powder particles are particularly like to lead to the nucleation of new grains, as seen in Fig. 36B-L.11.

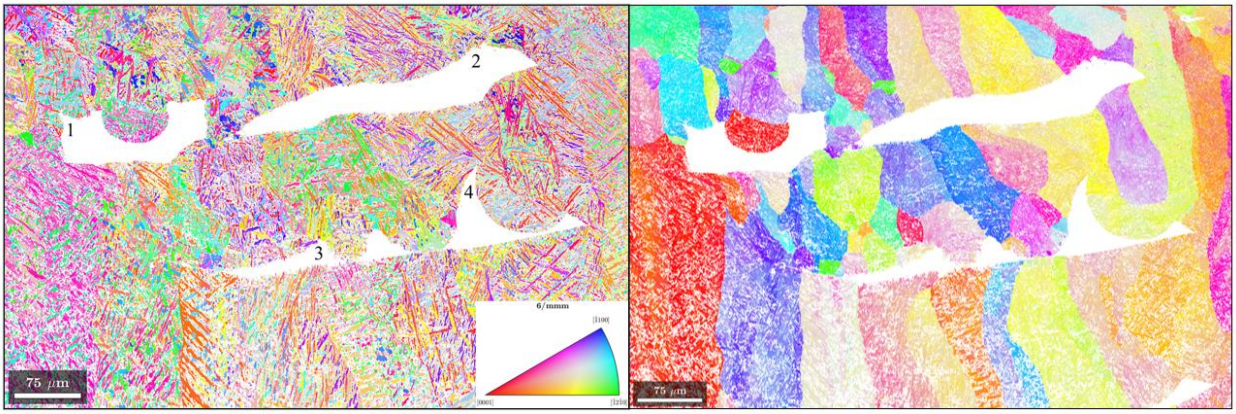

Figure 36BL.13. EBSD map around larger LOF defects and its parent grain reconstruction, showing nucleation of new grains from overhanging powder particles (notably, defects 1 and 3) as well as the continuation of some grains past defects (the right side of defect 2).

36B-L.4 Plans for Next Reporting Period

- Examine any existing correlation, or lack of a correlation, between local property variations and local compositional variations, through further nanoindentation experiments as well as microindentation.
- Expansion of FE modeling to account for additional variables and different mechanical properties, notably through the inclusion of plasticity into the model.
- Completion of search for evidence of retained gas porosity.
- Results published in 3-4 technical presentations, as well as an additional 1-2 manuscripts.

36B-L.5 References (See external document on references)

[36B-L.1] D. Du, J.C. Haley, A. Dong, Y. Fautrelle, D. Shu, G. Zhu, X. Li, B. Sun, E.J. Lavernia, Mater. Des. 181 (2019).
[36B-L.2] X. Wang, K. Chou, Addit. Manuf. 18 (2017) 1–14.
[36B-L.3] D. Dai, D. Gu, H. Zhang, J. Xiong, C. Ma, C. Hong, R. Poprawe, Opt. Laser Technol. 99 (2018) 91–100.
[36B-L.4] K.Z. Troost, P. Van Der Sluis, D.J. Gravesteijn, Appl. Phys. Lett. 62 (1993) 1110–1112.
[36B-L.5] B.L. Adams, J. Kacher, Comput. Mater. Contin. 14 (2009) 183–194.
[36B-L.6] T.J. Ruggles, D.T. Fullwood, Ultramicroscopy 133 (2013) 8–15.
[36B-L.7] S.S. Al-Bermani, M.L. Blackmore, W. Zhang, I. Todd, Metall. Mater. Trans. A Phys. Metall. Mater. Sci. 41 (2010) 3422–3434.
[36B-L.8] Y. Yang, PhD. Thesis, University of Pittsburgh (2015).
[36B-L.9] K. Unocic, M. Kirka, E. Cakmak, D. Greeley, A. Okello, S. Dryepondt, Evaluation of additive electron beam melting of Haynes 282 alloy, Materials Science and Engineering: A 772 (2020) 138607.
[36B-L.10] M.M. Kirka, F. Medina, R. Dehoff, A. Okello, Mechanical behavior of post-processed Inconel 718 manufactured through the electron beam melting process, Materials Science and Engineering: A 680 (2017) 338-346.

[36B-L.11] S.-W. Yao, T. Liu, C.-J. Li, G.-J. Yang, C.-X. Li, Epitaxial growth during the rapid solidification of plasma-sprayed molten TiO2 splat, Acta Materialia 134 (2017) 66-80.
[36B-L.12] A.S. Shaikh, F. Schulz, K. Minet-Lallemand, E. Hryha, Microstructure and mechanical properties of Haynes 282 superalloy produced by laser powder bed fusion, Materials Today Communications 26 (2021) 102038.
[36B-L.13] E. Chauvet, P. Kontis, E.A. Jägle, B. Gault, D. Raabe, C. Tassin, J.-J. Blandin, R. Dendievel, B. Vayre, S. Abed, Hot cracking mechanism affecting a non-weldable Ni-based superalloy produced by selective electron Beam Melting, Acta Materialia 142 (2018) 82-94.
[36B-L.14] W.J. Sames, F. List, S. Pannala, R.R. Dehoff, S.S. Babu, The metallurgy and processing science of metal additive manufacturing, International materials reviews 61(5) (2016) 315-360.